Journal of Inorganic and Organometallic Polymers and Materials
https://doi.org/10.1007/s10904-024-03176-3

RESEARCH

Zn-Doped WO_3 Nanomaterials: Bridging Experimental and COMSOL Assisted Analysis for Enhanced Photocatalytic and Antimicrobial Activity

Huma Tabassum[1] · Tahir Iqbal[1]

Received: 19 April 2024 / Accepted: 28 May 2024

Abstract
Photocatalysis is the most effective, economical, and environmentally friendly way to protect ecosystems and communities from the risks posed by the discharge of untreated wastewater containing dyes. This study reports the efficient degradation of MB dye for both pure and doped metallic nanoparticles. The hydrothermal technique was employed to synthesize pure and Zn-doped (1 to 4%) WO_3 NPs. The morphological, structural, optical, and spectral properties were investigated through the utilization of scanning electron microscopy (SEM), X-ray diffraction (XRD), ultraviolet–visible spectroscopy (UV–Vis), photoluminescence (PL), Fourier-transform infrared spectroscopy (FTIR) and EDX analysis. The well-matched ionic radius of Zn^{2+} with W^{+6} finds potential in dye degradations, because Zn^{2+} significantly contributes to the deceleration of the recombination rate of photogenerated electron/hole pairs resulting in subsequent reductions in band gap from 2.65 to 1.94 eV. For this investigation, MB dye was exposed to visible light to examine the photocatalytic activity of the synthesized NPs. It is worth mentioning that, the maximum degradation of 85% within 120 min attributed to the Burstein-Moss Effect indicates that 3% Zn-doped WO_3 catalyst exhibits the best results and the experiments involving trapping techniques have been performed to verify the stability of the optimized catalyst and the remarkable photocatalytic activity exhibited by the catalyst suggests its promising application in wastewater treatment. The synthesized nanomaterials have also been tested for antimicrobial activity. For better comprehension, a 2D model has also been simulated with the RF module of COMOSL Multiphysics 5.3a to correlate the experimental data with the theoretical findings.

✉ Tahir Iqbal
tahir.awan@uog.edu.pk

[1] Department of Physics, Faculty of Science, University of Gujrat, Hafiz Hayat Campus, Gujrat 50700, Pakistan

Published online: 15 June 2024

Graphical Abstract

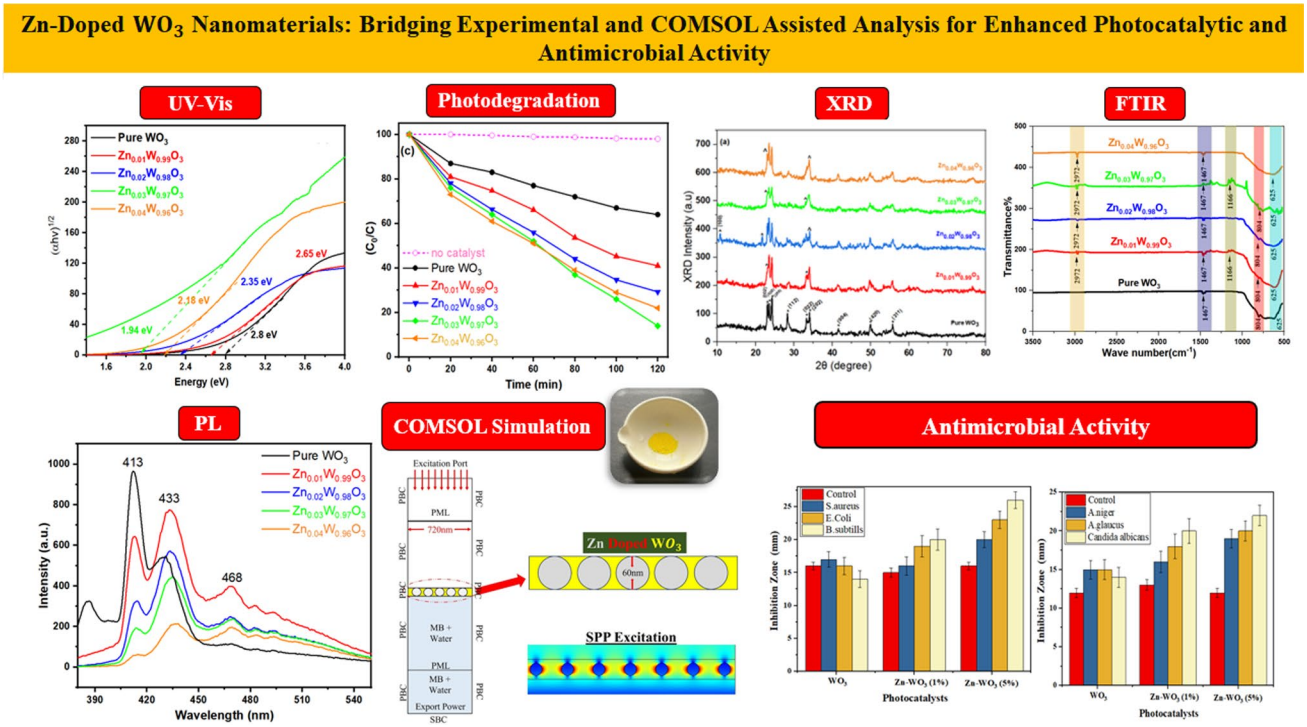

Keywords Photocatalyst · WO_3 · Zn-dopedWO_3 · Methyl blue · COMSOL · Antimicrobial activity

1 Introduction

Water serves a crucial role in sustaining life on earth because it is necessary for human survival [1]. Recently, notable emphasis has been directed towards the issue of water pollution. Environmental challenges related to water contamination have been a major problem in modern industrialized societies. Continuous industrialization and population expansion have led to an increase in energy consumption, which in turn has drawn significant attention to the environmental and water contamination issues [2]. Water pollution is the most significant challenge that is highly affecting humans and aquatic life. Modern industrialization is confronted with an immense ecological dilemma concerning the contamination of water resources. Unembellished water pollution is linked to dyes that cause significant health risks in today's world [3].

The industries utilize various materials such as dyes, cotton, synthetic fibers, and woolen fibers as raw materials. Approximately 10,000 synthetic dyes are available in the market, with a staggering annual production of over 7×10^5 tonnes worldwide [4–7].People all over the world are constantly exposed to various harmful contaminants. Air, food, and water are all contaminated by these harmful chemicals. Without adequate treatment, organic pollutants derived from sewage, animal waste, and industrial waste can harm aquatic organisms and microorganisms. Complexes containing azo makeup more than 70% of the dye family[8]. The textile business generates hazardous wastewater through various processing activities including printing, scouring, mercerizing, dyeing, and oxidizing, despite the industry's enormous economic benefits these processes have highly negative environmental and social effects. These textile wastewaters have been connected to several health conditions, including congenital anomalies, nausea, migraines, skin irritation, and skin rashes. Additionally, they have a detrimental impact on biodiversity, aquatic ecosystems, and receiving water bodies which is quite concerning [9].

Photocatalysis is an effective, economical, and environmentally beneficial method for wastewater treatment [10]. One of the greatest difficulties faced by the field of photocatalysis is to the pursuit for cost-effective, visible-light responsive, and environmentally friendly photocatalytic substances, particularly in the context of organic contaminant degradation [11, 12]. In recent years, the distinctive features of photocatalysts based on semiconductors, including their notable surface-to-volume ratio, distinct electronic properties, enhanced reactivity, and exceptional optical properties,

have gained significant attention among the scientific community as well as researchers [8].

Semiconductor photocatalysts hold great promise for addressing the pressing issues of the energy crisis and environmental contamination. Numerous photocatalysts, including $CeVO_4$/rGO [13], $Bi_2Mo\ O_6$ &Bi_2S_3 [14], TiO_2, CdS,WO_3, C_3N_4 [15], g-C_3N_4/Ag_2CO_3/GO [16], CdS/$CoMoS_x$, and $Nd_2Sn_2O_7$, among others, have been industrialized. However, their limitations arise from the fact that they can't concurrently achieve both a broad light absorption spectrum and a significant redox ability. Additionally, photocatalysts based on single-component often fails to meet the demands in real-world applications. Titanium dioxide (TiO_2) is intensively explored for water decontamination. However, the broad bandgap (3.30 eV), results in limiting conversion rates in the visible light range, poses a constraint on the use of titanium dioxide's (TiO_2) in photocatalysis. Photocatalysis involves the production of free radicals by a catalyst when exposed to light. These radicals then interact with pollutants, by degrading and converting organic contaminants into harmless substances. However, a significant obstacle is the photocatalyst's comparatively low visible light absorption capacity and high e^-/h^+recombination rate. Doping, composites, and heterojunctions are just few of the approaches a can be employed to effectively mitigate the bandgap and decrease the electron e^-/h^+ recombination rate [17]. Photocatalysts can be synthesized by variety of substances, encompassing organic compounds, metal oxides, sulphides, and various other materials. Tungsten oxide (WO_3) stands out as a good photocatalyst due to its extraordinary qualities, and exceptional attributes such as non-photo-corrosion, efficient electron transport properties, exceptional stability, and increased photoactivity, bandgap variation from 2.4 to 3.0 eV and comparatively high conductivity of about 12 $cm^2v^{-1}s^{-1}$. It is worth mentioning that the tungsten oxide valence band (VB) edge potential is primarily positive, indicating the material's enhanced photocatalytic oxidation activity [18–20]. WO_3 has remarkable photocatalytic properties, but rapid photogenerated electron–hole pair recombination during the photocatalytic process hinders it's widespread application [21]. In order to minimize charge carrier recombination rate, it is imperative to enhance photocatalytic performance of WO_3 based materials. Several investigations have been carried out to design and modify the WO_3 based nanostructure to improve its photocatalytic performance.

The biggest disadvantage of using TiO_2 and ZnO as a photocatalyst is wider bandgap and its absorption wavelength lies in the ultraviolet area which results in an excess of electron–hole recombination. Furthermore, ZnO has the ability to stimulate photochemical corrosion [22]. ZnO can have different photocatalytic properties depending on variety of factors such as the size, shape, and crystallinity of the particles. Photocatalytic activity can be enhanced through thermal treatment and/or metal ion doping by decreasing electron–hole pair recombination and increasing light absorption [23, 24]. Under the current water pollution scenario to enhance the cost-effectiveness of the catalytic process, it is necessary to develop and utilize catalysts that are active in the presence of solar light [25, 26].

This study reports that the enhanced photocatalytic and antimicrobial activity of hydrothermally synthesized WO_3 -based photocatalyst with varying Zn concentrations. Electrical and optical properties of WO_3 can be varied through the inclusion of Zn into WO_3 which entails the introduction of Zn ions into the lattice structure of WO_3 resulting into the formation of a composite structure known as Zn-doped WO_3. This structure has the potential to enhance specific characteristics rendering it advantageous for a energy storage, gas sensing, and photocatalysis applications.

This work involves the dual functionality of the synthesized Zn-doped WO_3 in terms of photocatalytic degradation and antibacterial activity. Our findings show that Zn-doped WO_3 has far more potential than pure WO_3 as a photocatalyst for decomposing MB dye when exposed to visible light. The novelty of this work is the comparative analysis to delve deeper into the mechanisms governing the photocatalytic activity by COMSOL Multiphysics simulations. These simulations were employed to model the interactions between Zn-doped WO_3 nanoparticles and specific molecules, such as Methylene blue. By employing this computational approach, a deeper understanding of the intricate processes involved and effective corroboration to experimental results can be attained.

The prepared catalysts will boost the morphology and crystallographic structure of the WO_3. In addition, the nanostructures' electrical, optical, and morphological features. Photocatalytic activities driven by visible light have been thoroughly studied and compared. The degradation of dye solutions [27] under visible light irradiation suggests the prepared catalyst will be useful for the degradation of industrial pollutants. Multiple techniques, including XRD, SEM, EDS, UV–vis, PL, and FTIR, are used to characterize utilized to examine the structural optical, and electronic characteristics of the synthesized catalyst. As a result, it provides scholars in this domain with novel insights to consider.

2 Experimental Methodology

2.1 Chemicals and Reagents

Sodium Tungstate Dihydrate ($Na_2WO_4.H_2O$) is the fundamental precursor that is used in the synthesis of WO_3. The base material is acquired from the University of Gujrat's chemical department. The physics department's nano lab

at the University of Gujrat provided the $Zn(NO_3)_2.6H_2O$ dopant and hydrochloric acid (HCl). The procedure was carried out using high-quality analytical reagents and chemicals. Throughout the experiment, only deionized or distilled water was utilized for the preparation of stock solutions. All chemicals utilized in this investigation were ≥ 99% pure and bought from Sigma Aldrich by the chemistry and physics departments.

2.2 Synthesis Method of Photocatalysts

WO_3 Nanoparticles (NPs) can be effectively synthesized by various methods, including hydrothermal, solvothermal, sol–gel, and green synthesis. The hydrothermal approach was selected for this investigation owing to the ability to yield NPs having strong crystallinity and a distinct morphological structure. Sodium tungstate dihydrate ($Na_2WO_4.H_2O$) was used as the precursor in a single-step hydrothermal method to synthesize pure WO_3 NPs [28, 29]. The first step involved stirring 1 g of ($Na_2WO_4.H_2O$) at 1500 rev/min for an hour with 100 mL of deionized water. A small amount (about 2 mL) of hydrochloric acid (HCl) was added to adjust the pH of the solution until yellow precipitates formed. The hydrothermal solution prepared around 70% of the total volume was then placed into a Teflon-lined autoclave and heated in an electric oven at 180 °C for 18 h. The resulting solution was then repeatedly washed with ethanol and double-deionized water to achieve a pH equilibrium. The solution was then dried in the oven for eight hours at 80 °C. The synthetic material was first dried, then calcined at 550 °C for two hours, and then coarsely crushed with a mortar and pestle. In the end, pure WO_3 NPs were obtained. WO_3 NPs were doped with Zn $(NO_3)_2.6H_2O$ at various concentrations ranging from 1 to 4%. For instance, 0.99 g of ($Na_2WO_4.H_2O$) in 100 mL of distilled water were doped with 1% by adding 0.01 g of Zn $(NO_3)_2.6H_2O$ dopant. The remaining steps for synthesizing Zn-doped WO_3 NPs followed a similar process as used to synthesize pure WO_3, with the appropriate proportions of Zn $(NO_3)_2.6H_2O$ dopant and ($Na_2WO_4.H_2O$) (see Fig. 1).

3 Characterizations

In this study the properties of Zn-doped WO_3 has been evaluated by employing different characterization techniques. The X-ray diffraction (JDX-3532-JEOL) method was employed to assess the crystallinity and purity of the synthesized nanomaterial. The morphology of the samples was examined using SEM (JSM5910-JEOL). A UV spectrometer (SP-IUV&, UOG) was used to compare the bandgap difference between pure WO_3 and Zn-doped WO_3 nanomaterials. An (FP-8200 JASCO) PL spectrometer was also utilized to observe the recombination rate of the electron–hole pair. The chemical characteristics were analyzed using FTIR spectroscopy (FT/IR-4100-A Jasco). The pure and Zn-doped WO_3 nanoparticles were used to test the photocatalytic activity and evaluate the degradation of methylene blue dye.

3.1 XRD Analysis

An XRD (JOEL-JDX-3532) was used to conduct XRD analysis. Figure 2 shows the XRD patterns of pure WO_3 and Zn-doped WO_3 NPs monoclinic structure and in accordance to the JCPDS data card (JCPDS 43–1035), the observed diffraction peaks are in agreement with the monoclinic structure of WO_3 [30]. The monoclinic WO_3 has planes (0 0 2), (0 2 0), (2 0 0), (1 2 0), (1 1 2), (2 1 2), (0 3 2), (0 0 4), (1 4 0) and (2 4 0) were attributed to the diffraction peaks at 2 θ=23.06°, 23.54°, 24.26°, 26.57°, 28.92°, 28.31°, 42.43°, 50.04° and 52.3°. Pure WO_3 had the following lattice parameters: a = 7.3090 (Å), b = 7.5220(Å), c = 7.6780 (Å), and α = 88.8100, β = 90.9200 γ = 90.9300. It suggests that the films are well-crystalline and show a strong preference orientation (200), which is supported by a prominent high-intensity peak for (1–4%) doping that is located at about 26.57°. For Pure WO_3, the average crystalline size is 75 nm nm, and it dropped for higher Zn concentrations (1–4%). An increase in Zn concentration resulted in a decrease in peak crystallinity. The decrease in peak intensities with the doping level provides another confirmation to decrease in crystallinity with Zn doping. Zn^{2+} had an ionic radius of 0.74 Å while W^{6+} had a radius of 0.60 Å [31]. It is anticipated that some Zn^{2+} will displace some W^{6+} during doping without varying its monoclinic crystal structure. This might be attributable to the film experiencing macrostrain during doping. The average crystallite size was calculated using Sherrer's equation [32].

$$D = \frac{K\lambda}{\beta Cos\theta} \tag{1}$$

Therefore, the XRD pattern "*" depicts the WO_3 peaks and "^" slight peak shift owing to varying doping concentrations, but the general crystallographic structure remains the same.

The microstrain was calculated by the Williamson-Hall method [33].

$$\beta\cos\theta = (4\varepsilon\sin\theta) \tag{2}$$

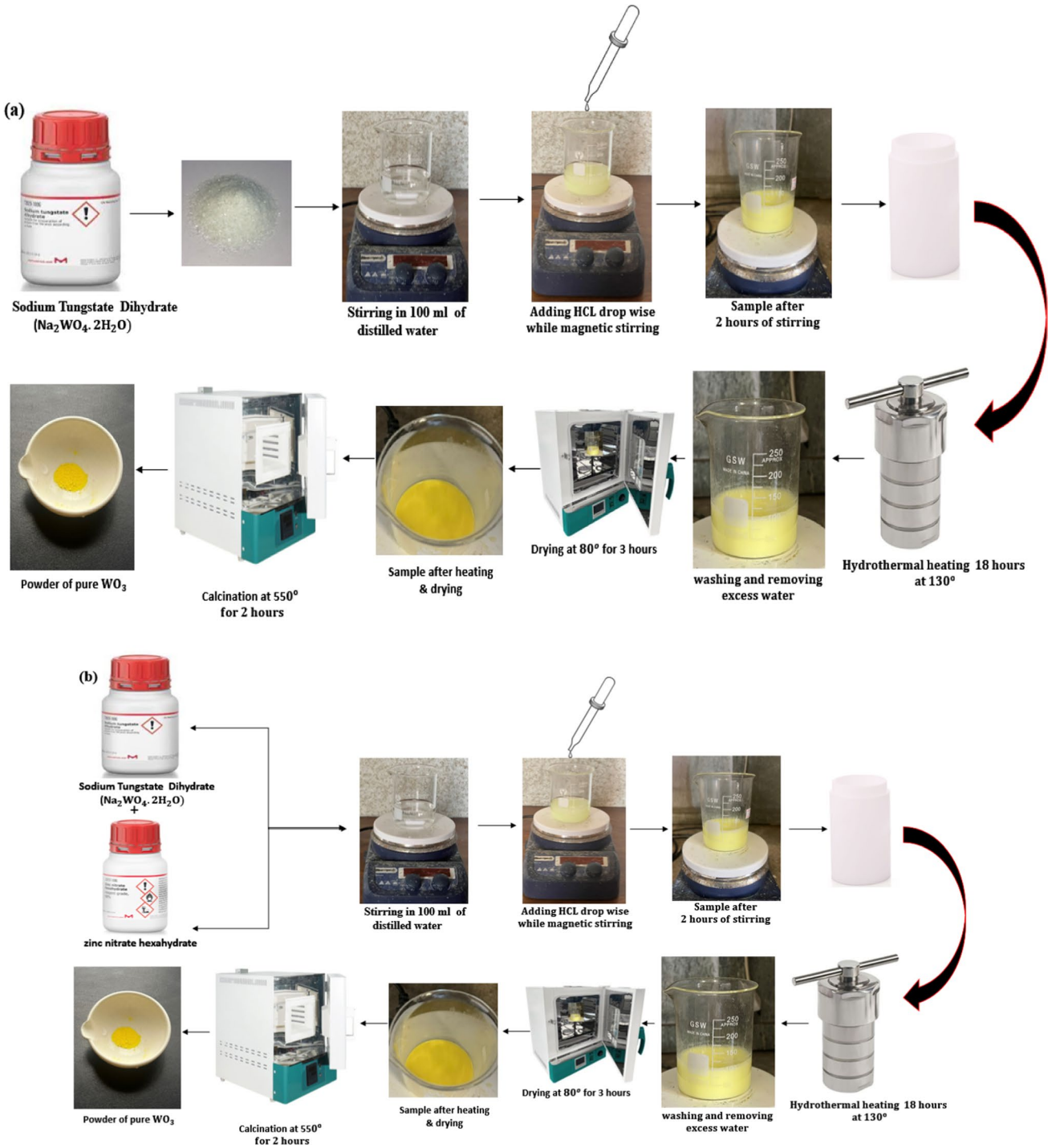

Fig. 1 **a** A schematic diagram illustrating the hydrothermal synthesis process for the synthesis of Pure WO_3 nanoparticles. **b** Schematic depiction of the hydrothermal synthesis process utilized for the preparation of Zn-doped WO_3 nanoparticles

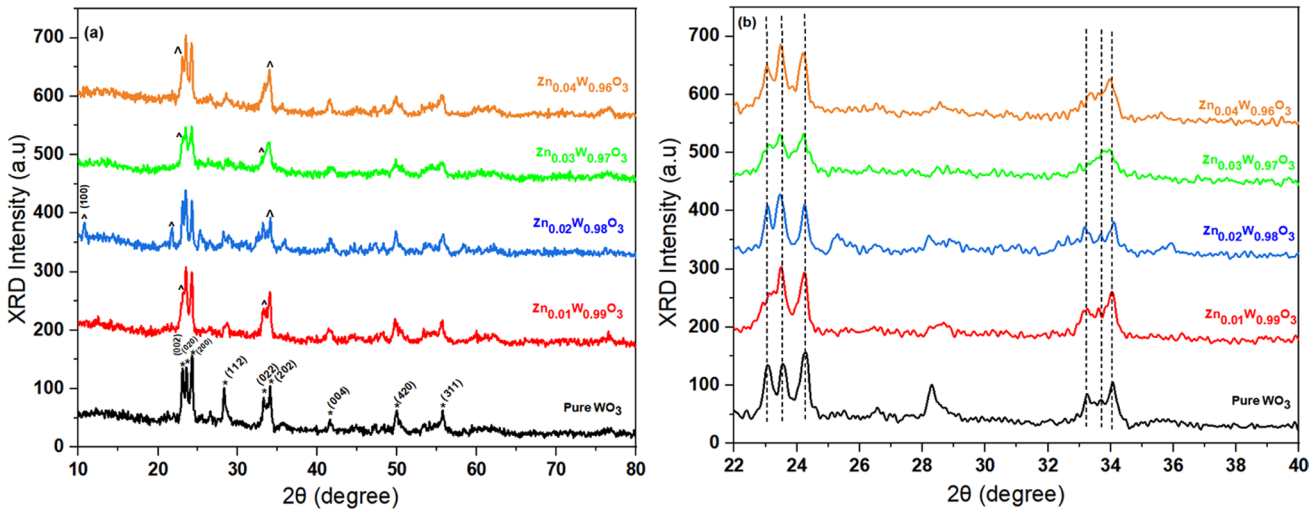

Fig. 2 **a**, **b** XRD spectra depiction of WO_3 and Zn − doped WO_3 of phase shift and slight intensity reduction

Table 1 The calculated crystallite size, Microstrain (ε) and dislocation density (δ) by XRD analysis and E_g by UV–VIS analysis of Pure and Zn-doped WO_3

Synthesized sample	Crystaline size (nm)	Micro strain $(\varepsilon) \times 10^{-4}$	Dislocation density $(\delta) \times 10^{-4} lines/nm^2$	Energy band gap $E_g(eV)$
Pure WO_3	75	14.26	1.777	2.8
$Zn_{0.01}W_{0.99}O_3$	69	35.11	2.1	2.56
$Zn_{0.02}W_{0.98}O_3$	58	38.19	2.9	2.35
$Zn_{0.04}W_{0.96}O_3$	42	72.29	5.668	1.94
$Zn_{0.03}W_{0.97}O_3$	43	64.48	5.408	2.18

$$\varepsilon = \frac{\lambda}{DSin\theta} - \frac{\beta}{tan\theta} \tag{3}$$

Dislocation density in relation to crystallite size can be calculated by following the equation below:

$$\delta = \frac{1}{D^2} \tag{4}$$

The determined dislocation density, energy band gap, microstrain, and crystallite size values in Table 1.

3.2 SEM

An SEM analysis has been performed using a JSM5910-JEOL, operating at an acceleration voltage of 30 kV. The Prepared Pure and Zn doped $-WO_3$ NPs exhibits distinct morphologies, with a combination of both spherical and rod-shaped structures. Additionally, these particles exhibit a remarkably low level of aggregation. The majority of the particles were spherical and were investigated using Image J software [34]. There were irregular shapes with grain sizes ranging from 42 to 75 nm, although the average grain size was considered to be 45 nm. SEM analysis revealed significant details about the shape of the pure $WO_3$and optimal 3% Zn-doped WO_3 NPs at different magnifications (Fig. 3). It is worth mentioning that particle size and shape were thus found to be highly influenced by Zn concentration and have significant effect on synthesized NPs which indicates that the morphology of the material could potentially be modified by varying the dopant concentrations. More specifically, the Zn-doped WO_3NPs exhibited a more homogeneous shape and smaller particle sizes at higher 3% Zn concentrations. Additionally, it was noted that changes in microstructure under various operational conditions had a notable effect on the activity and selectivity of the synthesized NPs [35]. High levels of aggregation and disorder morphology were seen in the surface morphology of Zn-doped WO_3 NPs synthesized by other researchers using different techniques [36–39]. Pure WO_3 undergoes morphological changes due to the presence of Zn ions in to the lattice. Figure 4(a, b) shows the EDX graphs, containing the weight and molarity percentage of the pure and Zn-doped WO_3.

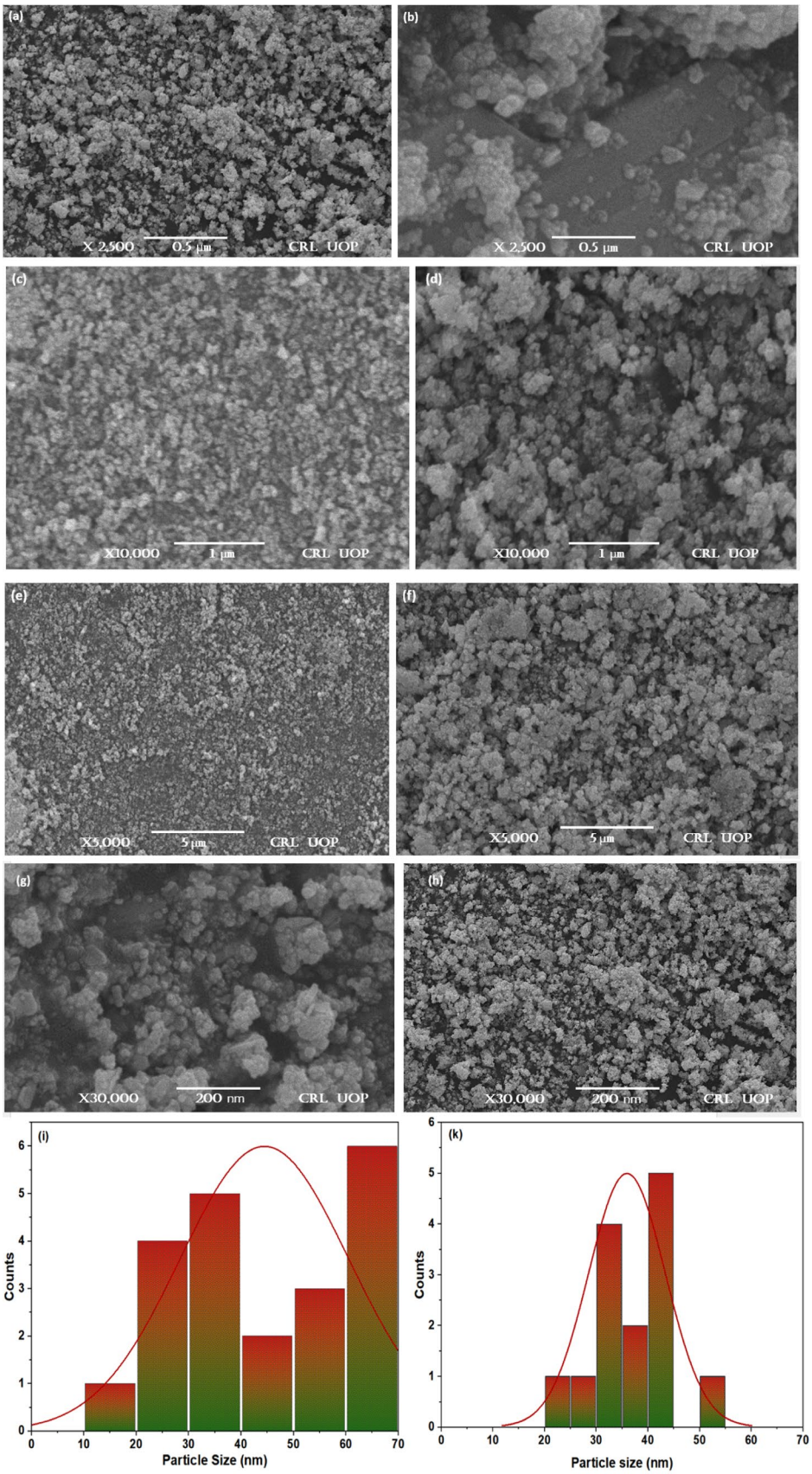

Fig. 3 **a**, **c**, **e**, **g** SEM images of pure WO_3, **(b**, **d**, **f**, **h)**. SEM images of 3% Zn-doped WO_3 nanoparticles**,** **(i**, **k)** Histogram plots depict the average size of WO_3 and Zn-doped WO_3 NPs

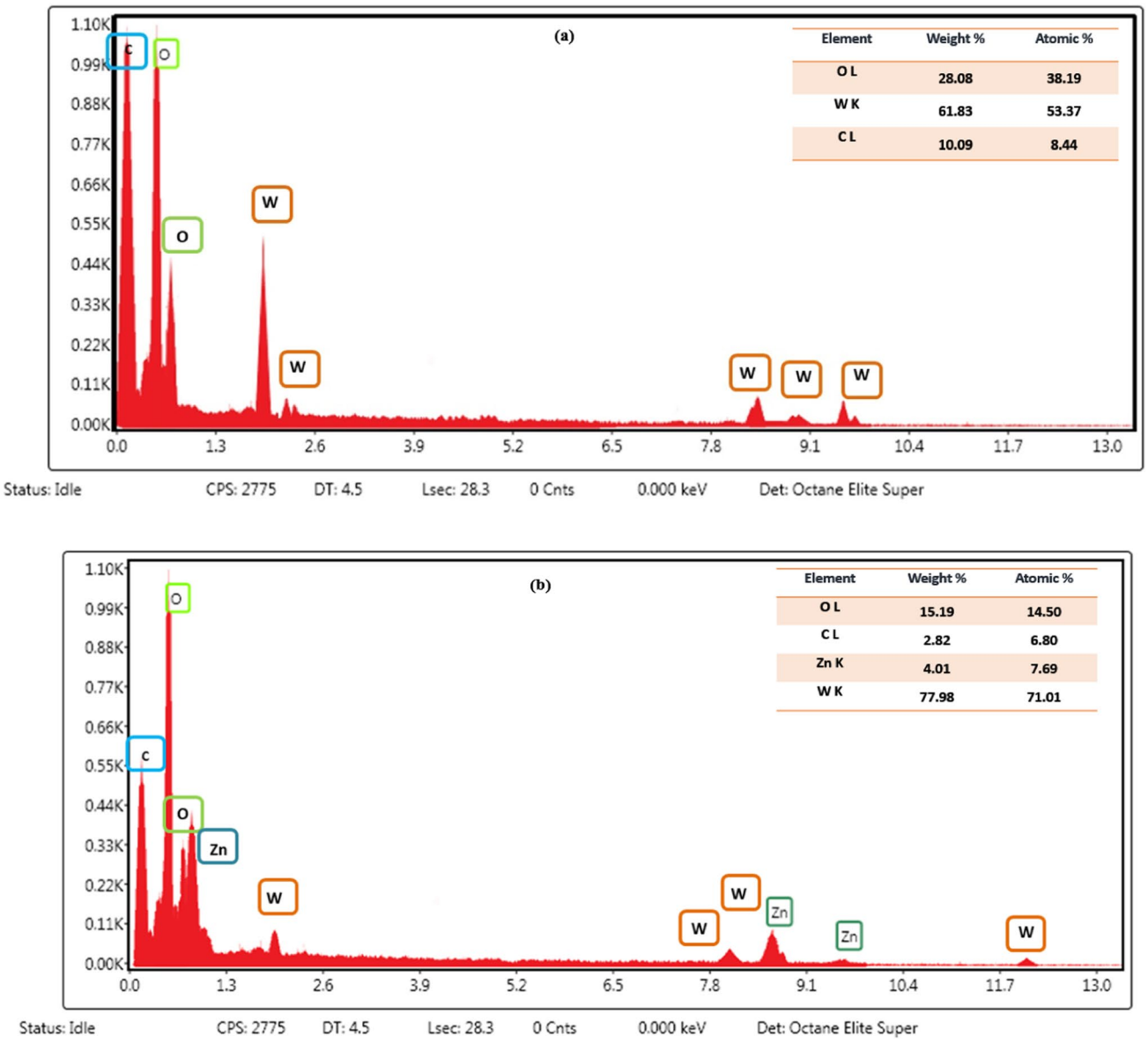

Fig. 4 **a**, **b** Depiction of EDX analysis along with the atomic % and molar % of WO_3 and 3% Zn-doped -WO_3

3.3 UV–Visible Analysis

A double-beam UV–Vis Spectrophotometer (model SP-IUV&UOG) was used to measure the UV–Vis spectra of both pure and Zn-doped (1%, 2%, 3%, and 4%) WO_3 NPs. The optical band gaps and defects in these materials depend on the absorbance characteristics. The band gap values were calculated using Tauc plots, yielding 2.8 eV for pure WO_3 and (2.66, 2.35, 1.94, 2.18) eV for (1–4) % Zn-doped WO_3, respectively, in direct transitions (as shown in Fig. 5).

Interestingly, the band gap decreases when Zn was added to WO_3 at 1%, 2%, and 3%, but it increased once again at 4% Zn doping, demonstrating the presence of Zn^{+2} ions within the WO_3 lattice. This phenomenon can be related to the Burstein-Moss effect, which, at a particular concentration of impurity atoms, causes the Fermi energy level to shift towards the valence band, producing a blue shift and an increase in the visible band gap of the semiconductor material. As a result, it is determined that 3% Zn doping in WO_3 is more effective than other concentrations of doping.

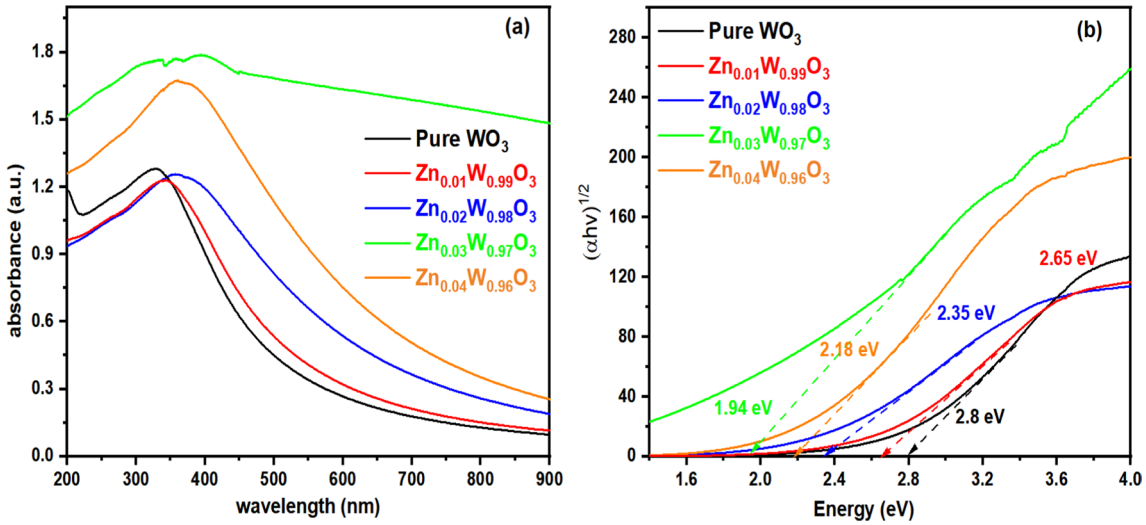

Fig. 5 **a**, **b** UV–vis spectroscopy measurements band gap values for direct transitions for pure and Zn-doped WO_3

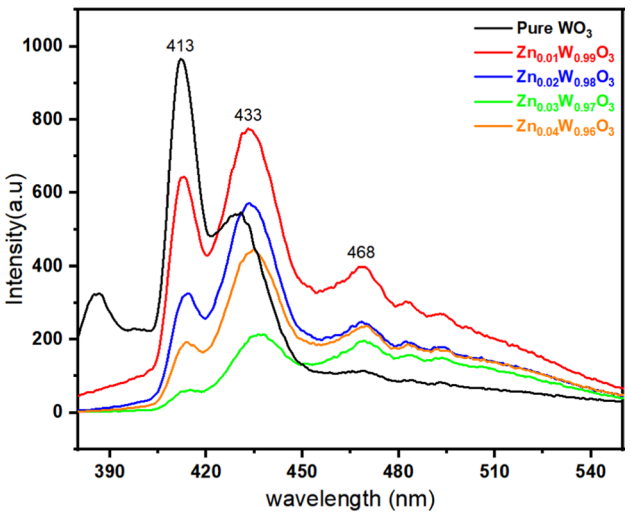

Fig. 6 Pure and Zn-doped WO_3 PL spectra measurements

In addition, the WO_3 nanoparticles experience phase changes as a result of the rise in doping levels, which causes electron stimulation and excitation to move from the valence band (VB) to the conduction band (CB).

3.4 PL Analysis

Through PL spectroscopy (PL: RAMANLOG 6, UOG), optical characteristics of the prepared samples, such as change in intensity and recombination rate of photo-generated electron/hole pairs, and material defects, have been found as shown in Fig. 6. The excitation wavelength for the PL spectroscopy was 320 nm. The two regions of the PL spectrum are the UV region, which has a band gap peak, and the broadband spectrum region, which contains peaks of structural defects [40]. A higher PL intensity is frequently indicative of the material's maximum rate of recombination of photogenerated e^-/ h^+ pairs. Pure WO_3 exhibits wider, more intense emission peaks with a center at 413 nm than doped WO_3, indicating significantly faster rate of recombination of e^-/h^+.

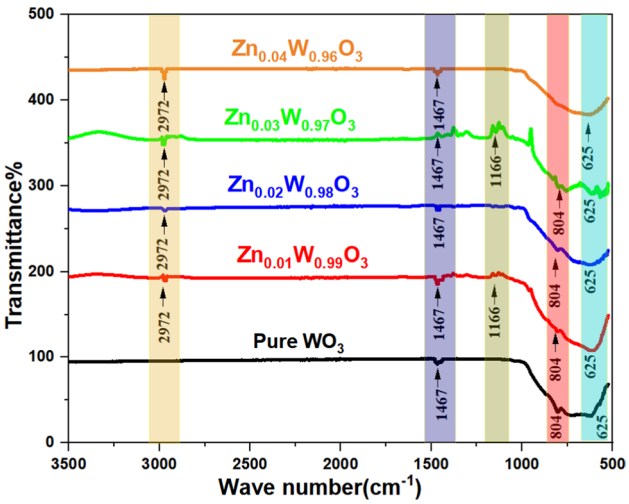

Fig. 7 FTIR spectral measurements of pure and doped WO_3 at various Zn concentrations

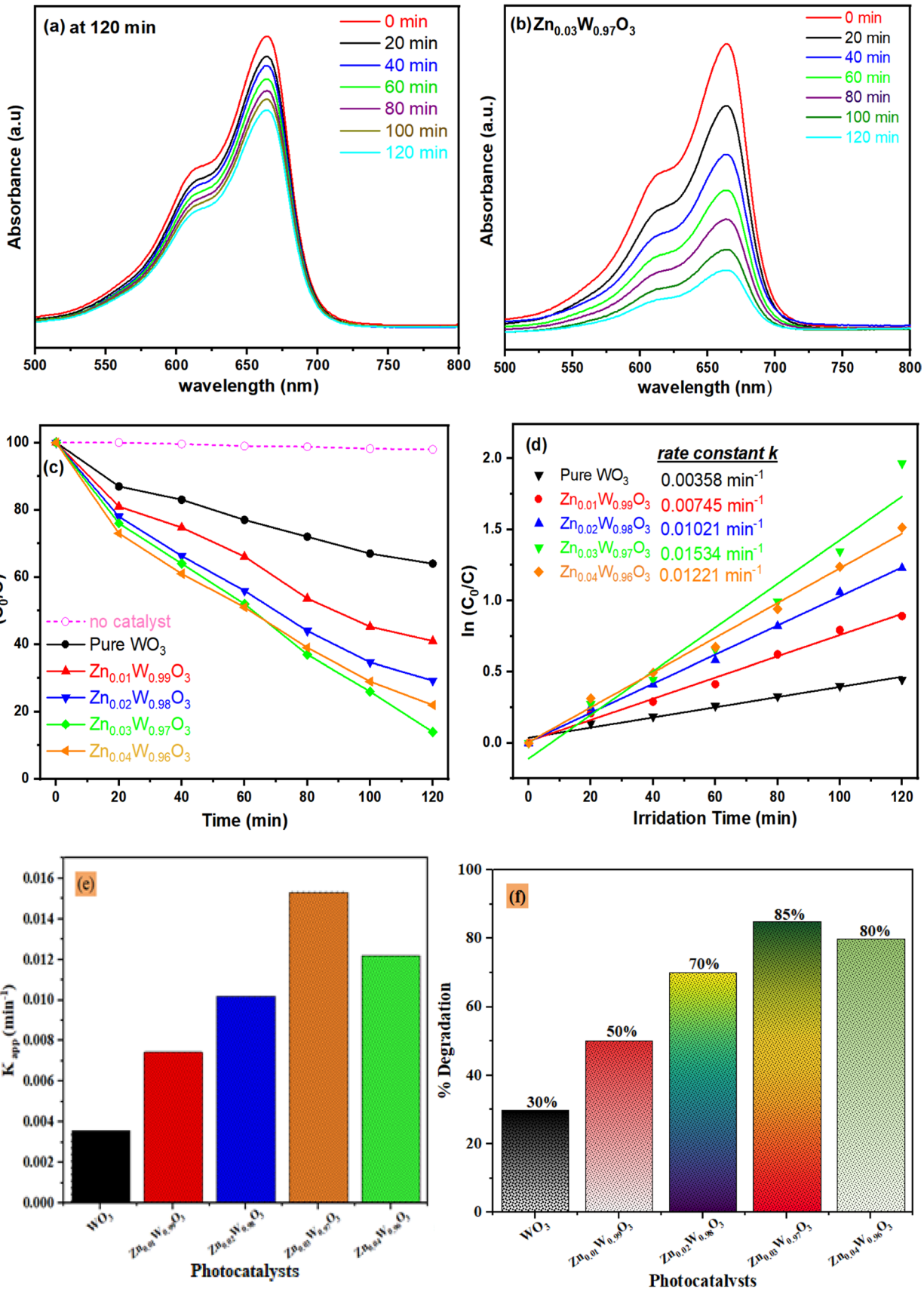
(a) at 120 min
0 min
20 min
40 min
60 min
80 min
100 min
120 min
Absorbance (a.u)
wavelength (nm)
(b) Zn0.03W0.97O3
0 min
20 min
40 min
60 min
80 min
100 min
120 min
Absorbance (a.u.)
wavelength (nm)
(c)
no catalyst
Pure WO3
Zn0.01W0.99O3
Zn0.02W0.98O3
Zn0.03W0.97O3
Zn0.04W0.96O3
(C0/C)
Time (min)
(d)
rate constant k
Pure WO3 0.00358 min-1
Zn0.01W0.99O3 0.00745 min-1
Zn0.02W0.98O3 0.01021 min-1
Zn0.03W0.97O3 0.01534 min-1
Zn0.04W0.96O3 0.01221 min-1
ln (C0/C)
Irridation Time (min)
(e)
Kapp (min-1)
WO3
Zn0.01W0.99O3
Zn0.02W0.98O3
Zn0.03W0.97O3
Zn0.04W0.96O3
Photocatalysts
(f)
% Degradation
30%
50%
70%
85%
80%
WO3
Zn0.01W0.99O3
Zn0.02W0.98O3
Zn0.03W0.97O3
Zn0.04W0.96O3
Photocatalysts

◂**Fig. 8** **a** The UV–Vis spectrum of pure and 1–4% Zn-doped WO_3 at 90 min for photocatalytic activity. **b** Double beam spectrum UV–Vis for the highest optimized concentration of photocatalytic activity 3% Zn-doped WO_3 for an hour. **c** Degradation efficiency with respect to time for Zn-doped and pure WO_3 nanoparticles. **d** First-order kinetics of both doped and pure WO_3 nanoparticles. **e** rate constants of pure and 1–4% Zn-doped WO_3. **f** Degradation % of pure 1–4% Zn-doped WO_3NPs

The persistent 425 nm shoulder peak represents oxygen vacancies and the persistent presence of defects in the crystal lattice in both pure and Zn-doped WO_3 samples. The absence of the 380 nm peak in Zn-doped WO_3 is associated to the fact that changes arise from differences in electronic transitions and recombination processes as Zn can have an impact on energy levels within the bandgap, leading to changes or reductions in certain peaks in PL spectra, such as at 380 nm. In terms of the existence of a peak at 468 nm after Zn doping, is attributed to the fact of changes in the photocatalyst's surface states or electronic structure resulting in doping-induced surface defects. Quality of absorption and emission can be improved by the Zn doping into WO_3 as it creates new energy levels within the bandgap. Doping has decreased the electron–hole recombination rate by trapping the photo-electrons, as seen by the intensity of PL peaks decreasing with increasing dopant concentration. Low recombination rate suggests that there are more free charge carriers available than needed for the photocatalytic degradation process.

3.5 FTIR Analysis

The FTIR spectral analysis involved the evaluation of WO_3 and Zn-doped WO_3 nanostructures at different concentrations (1%, 2%, 3%, and 4%) within the 4000–500 cm^{-1} region. The spectrum analysis reveals a wide absorption band, providing strong proof of WO_3 existence at room temperature. The stretching vibrations of W-O-W and O-W-O bonds are linked to the spectral features detected at 625 cm^{-1} and 804 cm^{-1}, respectively. Furthermore, the stretching vibrations of the C-O bonds are suggested by the peaks at 1166 cm^{-1}, whereas the bending vibrations of the H–O–H bonds corresponds to the peaks at 1467 cm^{-1}. It is worth mentioning that the existence of Zn doping in pure WO_3 has been confirmed by the observation that the low concentration of Zn dopant corresponds to the minimum peaks at 625 cm^{-1} and 804 cm^{-1} which indicates the stretching vibrations of the O-3 Zn and Zn-O-Zn bonds as shown in Fig. 7.

4 Photocatalytic Activity

A 400 W high-powered metal halide lamp capable of emitting visible light with a wavelength ≥ 400 nm and a maximum operating temperature of 1000 °C was utilized for visible light radiation to examine the effectiveness of dye degradation in synthesized materials. Catalytic activity depends on the photocatalyst's contact time and the other critical characteristics include the band gap, recombination rate of electron–hole pairs, morphology and dimensions, temperature, and concentration of pollutants. In general, WO_3 was thought to be a particularly potent photocatalytic catalyst.

A 10-ppm dye solution is prepared using distilled water. A 0.1 mg photocatalyst is added to 100 mL of dye solution in each sample. The mixture is then subjected to 20 min of stirring in the absence of light to achieve equilibrium. This experimental setup allows us to examine the effects of adsorption during the initial 20-min period. The suspension is then exposed to daylight for 120 min. The solution's decolonization demonstrates photocatalytic activity. A 5 ml sample of the solution was collected at 20-min intervals and subjected to analysis utilizing a UV–Vis double beam spectrophotometer. This procedure was repeated 120 times. The same approach was followed for Zn-doped WO_3 catalysts and the dye removal (100 ml of a 10-ppm solution) has been monitored over time and the catalytic efficiency of dye removal is determined using Eq. (5), as illustrated in Fig. 8.

$$\text{Degradation Efficiency } (\%) = \left(1 - \frac{C}{C_o}\right) \times 100 \tag{5}$$

$$\text{Rate Constant (K)} = \ln\left(\frac{C_o}{C}\right) t \tag{6}$$

where C_o represents the initial concentration, while C represents the concentration of the dye at a given time t. In Fig. 8a, the UV–Vis spectra of pure and Zn-doped WO_3 in MB dye after 120 min are presented. The observed downward shift in the absorption peak as the time interval increases suggests the degradation of MB. For this purpose, 20 min is absorption–desorption time for equilibrium. Then, degradation activity of methylene blue [27] was observed for 120 min with a difference of 20 min duration i.e., 20, 40, 60, 80, 100, and 120 min without presence of the catalyst, with pure WO_3 and series of doped WO_3 with Zn variation 1%, 2%,3%,4%. The degradation activity is shown in Fig. 8b. This shows that when there is no catalyst present no degradation is observed.

Table 2 Comparison of current study with previously published in the literature

Sr. no	Photocatalyst	Methodology	Model pollutant	Degradation%	References
1	Mo	Hydrothermal	Methylene orange	86.1	[42]
2	Mn	Hydrothermal	MB dye	79	[43]
3	Pr^{3+}	Co-precipitation	Crystal violet	73	[44]
4	Boron	CO-precipitation	MB	93.4	[45]
5	Zn-doped WO_3	Hydrothermal	MB	85	Current study

In Fig. 8, for WO_3 after 120 min, 30% MB is degraded while 70% remains undegraded. For 1% Zn doped WO_3 after 120 min 50% MB undegraded and 50% degraded. Zn-doped WO_3 2% has degraded 70% MB and 30% undegraded. MB is 85% degradation occurs for the Zn 3% doped in WO_3 while 15% remain undegraded. The WO_3 doped with 4% Zn undegraded 20% MB and degraded 80%. The doped WO_3 has a greater degradation performance in comparison to pure WO_3. This analysis shows that the optimum 85% degradation of MB was achieved after 120 min with the 3% Zn doped WO_3 shows higher degradation efficiency as compared to the other doped 1%,2%,3%, and 4% WO_3 and the comparison of current study degradation with previously reported has been shown in Table 2. The absorption graph with respect to time also shown in Fig. 8c. But gradually when the time increased the absorption decreased respectively from 30 to 120 min. As absorption decrease it represents concentration of dye decreases which illustrates dye is degraded with photocatalytic material of Zn-doped WO_3.

Additionally, the results are subjected to first-order kinetics. This allows the calculation of the rate constant using Eq. (6) and the evaluation of the correlation coefficient R^2, which is optimal for 3% Zn-doped WO_3 nanoparticles and represents the level of linear correlation between different quantities, through linear fitting using Origin 2021 (Fig. 8). Furthermore, upon exposure to light of a specific frequency, the photocatalyst undergoes excitation, leading to the activation of valence band electrons. The electrons subsequently undergo shift towards in the direction of the conduction band, resulting to the generation of an equal number of holes in the valence band as has been observed [41]. As illustrated in Fig. 9, a system containing WO_3 ions can absorb photogenerated electrons. This process produces reactive oxygen species including singlet oxygen, superoxide anion radical, hydrogen peroxide, and hydroxyl ions [15]. The following are the mathematical expressions:

$$Zn/WO_3 + hv \rightarrow Zn/WO_3(e^-) + Zn/WO_3(h^+) \quad ((i))$$

$$Zn/WO_3(h^+) + MB(dye) \rightarrow MB^+(dye) + Zn/WO_3 \quad ((ii))$$

$$Zn/WO_3(h^+) + H_2O \rightarrow Zn/WO_3 + OH^- + H^+ \quad ((iii))$$

$$Zn/WO_3(h^+) + OH^- \rightarrow Zn/WO_3 + OH^{\cdot} \quad ((iv))$$

$$Zn/WO_3(e^-) + O_2 \rightarrow Zn/WO_3 + O_2^{\cdot -} \quad ((v))$$

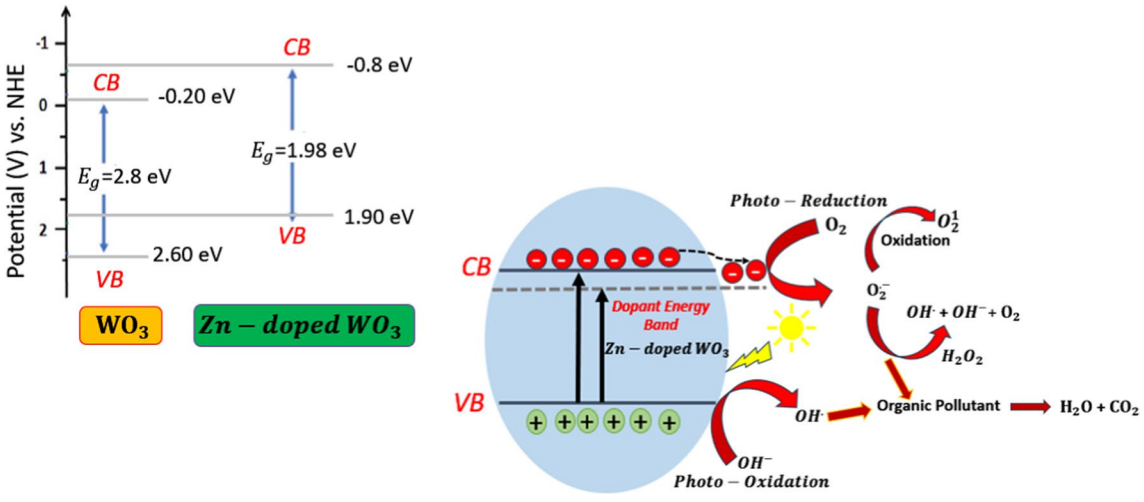

Fig. 9 Graphical depiction of the band structure of Zn-doped WO_3, computed through the investigation of valence band edge effects, electrochemical, and optical phenomena

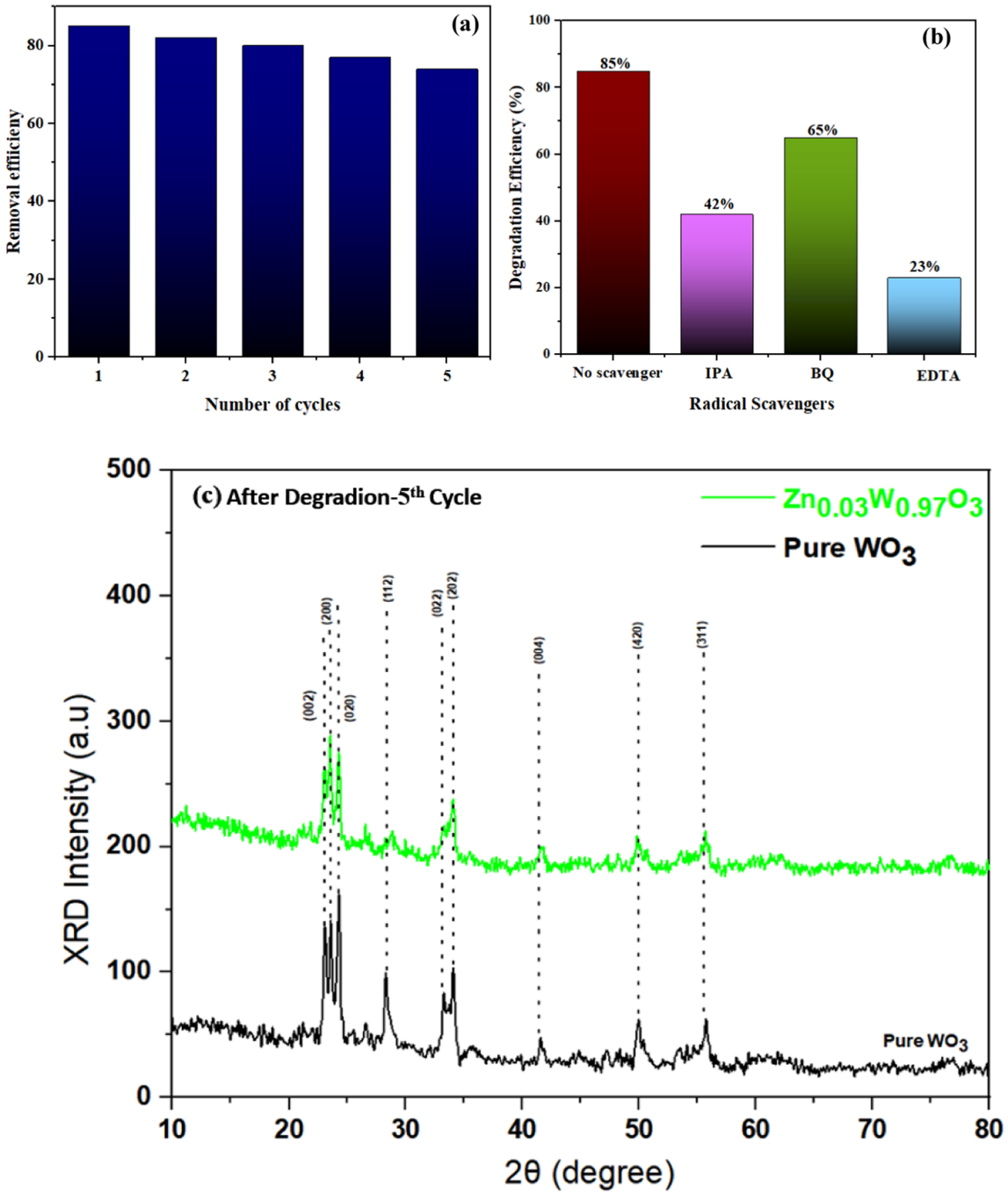

Fig. 10 **a** Demonstrating the five cycles of MB degradation using an optimized 3% Zn-doped WO_3 catalyst's stability. **b** Impact of distinct radical scavengers on 3% Zn doped- WO_3 catalytic performance. **c** Post Photocatalysis XRD after 5-cycles

$$O_2^{\cdot -} + e^- + 2H^+ \rightarrow H_2O_2 \quad \text{((vi))}$$

$$O_2^{\cdot -} + H_2O_2 \rightarrow OH^{\cdot} + OH^- + O_2 \quad \text{((vii))}$$

$$O_2^{\cdot -}/OH^{\cdot} + \text{dye} \rightarrow CO_2 + H_2O \quad \text{((viii))}$$

4.1 Recyclability

Recyclability was studied as a measure of the photocatalyst's stability because it is significant from an application perspective. After use, the 3% Zn-doped WO_3 catalyst was retrieved by evaluating its stability in this experiment. In the photochemical experiment, the material was repeatedly rinsed with water and acetone to get rid of unwanted material. Afterward, it was dried at 80 °C for 3 h before being used in the following experiment. After the incorporation of an additional five instances of 3% Zn-doped WO_3 for the purpose of degrading MB, the % of dye degradation, as depicted in Fig. 10a, exhibits slight decrease in the catalyst's photocatalytic efficiency and this observation suggests the substance's improved photocatalytic stability. Figure 10c displays the XRD analysis of the WO_3 and Zn-doped WO_3 after the five cycles of MB dye degradation. The durability, recyclability and improved photocatalytic efficiency of the synthesized WO_3 and Zn-doped WO_3 were proven by the fact that the photocatalyst maintained its efficiency even after five cycles, showing only a slight decrease in intensity. Furthermore, the post-photocatalysis XRD analysis after five cycles offers unambiguous proof of the purity of the synthesized nanomaterials.

4.2 Radical Scavenger Effect

Radical capture tests were conducted. The production of the superoxide radical $\bullet O_2^-$, holes (h^+), and hydroxyl radical •OH within the reaction mixture upon excitation of semiconducting material has been reported to be trapped by different scavengers, such as isopropyl alcohol [34], ethylenediaminetetraacetic acid (EDTA) and p-benzoquinone (BQ). In order to get better insight into the photocatalytic mechanism and to investigate how the primary reactive species affect the mechanism of photocatalytic degradation the variation in MB concentration as a function of irradiation duration is shown in Fig. 10b both in the absence and presence of different scavengers, including 3% Zn-doped WO_3 photocatalyst. The findings demonstrate that $\bullet O_2^-$ and •OH are the primary reactive species involved in the breakdown of MB and scavengers like EDTA and BQA have a considerable impact on decreasing the degradation rate.

4.3 Effect of pH and Catalyst Loading on MB Dye

For the purpose of studying the degradation of MB, the effect of catalyst loading was performed using 3% Zn-doped WO_3 catalyst. Figure 11a shows the degradation percentage against catalyst loading. The results of the analysis indicate that a specific quantity of catalyst is appropriate for all Photocatalytic activity. While the quantities of generated charge carriers increase with catalyst quantity, a uniform trend of enhanced photocatalytic activity by catalyst amount has been observed. In the case study of MB dye, we observed that a quantity of 0.10 g/L reveals the maximum photodegradation of MB dye. In order to reduce the photocatalytic activity, a high concentration of catalyst is required, as this prevents the catalyst from aggregating and also eliminates the poisoning effect. The degrading efficiency decreased as the catalyst concentration increased to 0.2 g/L.

The amount of catalyst influences the efficiency of degradation. Its decomposition- and essentially stable nature makes it a better potential applicant for photocatalytic activity. The maximum amount of degradation of the MB dye occurs at a pH of 9. The removal efficiencies of 50%, 51%, 71%, 85% and 78% of MB were obtained at pH 6, pH 7, pH 8, pH 9 and pH 10, respectively (Fig. 11b). At pH 9, the maximum efficiency was attained. Figure 11b displays a graph of degradation % at different pH values and 11 c shows pHzpc(Zeta Potentional) graph of WO_3 and Zn-doped WO_3.

5 COMSOL Simulation

The 2D experimental work's model is simulated using COMSOL Multiphysics 5.3a. Figure 12 depicts the schematics. Various boundary conditions have been implemented in order to imitate the conditions of the experiment. The 2D model is excited by UV–visible to near-infrared radiation (NIR) via an input port. To make sure that the radiations have an even distribution, scattering boundary conditions, or SBCs, are employed. Periodic boundary conditions (PBC) are applied to the model's boundaries on the left and right, while continuous boundary conditions (CBC) are applied to the model's interior boundaries and the boundary conditions equations (Eqs. 7, 8, 9) are listed below.

$$E_{dst} = E_{src} \exp\left(-jk.\left(r_{dst} - r_{src}\right)\right) \tag{7}$$

$$\left(\mathrm{n} \times \left(H_1 - H_2\right)\right)_z = 0, \left(n \times \left(E_1 - E_2\right)\right)_z = 0 \tag{8}$$

$$n \times \left(\nabla \times A_z\right) - jkA_z = -jk(1 - k.n)A_{0z} \exp\left(-jk.r\right).A = EorH \tag{9}$$

The model is meshed first Prior to normalization. As shown in Fig. 12, the simulated WO_3 particle size (experimental value) was 60 nm. WO_3 NPs had been immersed in Rh Band water solution during the 200-min simulation. Using 1 nm step size, for optimum outcomes, the wavelength

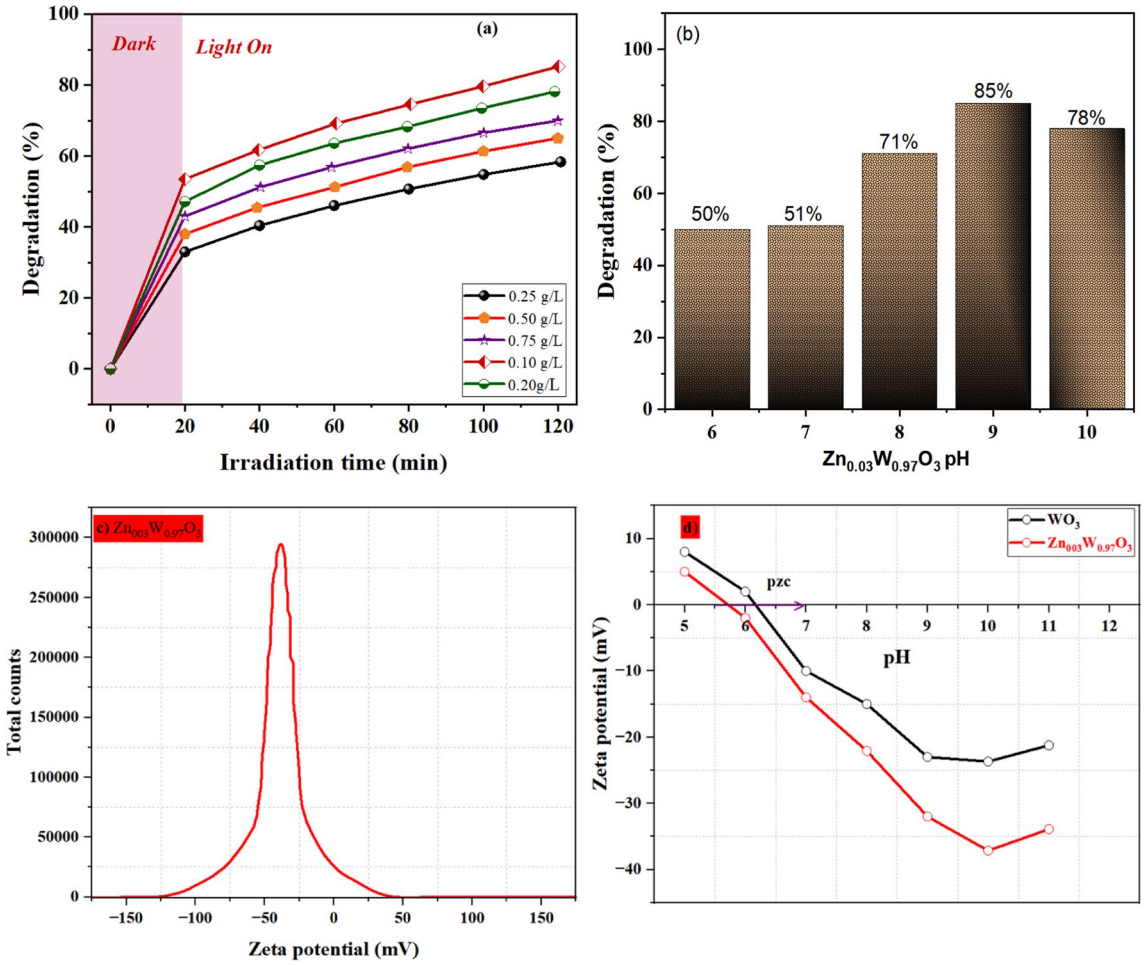

Fig. 11 **a** Effect of catalyst loading on MB degradation by using 3% Zn-doped WO_3. **b** Effect of pH on MB degradation by using 3% Zn-doped WO_3. **c**, **d** pHZpc graph of $WO_3$and 3% Zn-doped WO_3

has been swept from 300 to 1000 nm. The simulation has made use of TM polarized light. The following are the Maxwell equations (Eqs. 10, 11, 12) governing the light-matter interaction.

$$\nabla \times \left(\mu_r^{-1} \nabla \times E\right) - \left(\varepsilon_r - \frac{i\sigma}{\omega\varepsilon_0}\right) K_0^2 E = 0 \tag{10}$$

$$\nabla \times \left((\varepsilon_r - \frac{i\sigma}{\omega\varepsilon_0})^{-1} \nabla \times H\right) - \mu_r K_0^2 H = 0 \tag{11}$$

$$E = E_z e_z, H = H_z e_z, \varepsilon_r = n^2 \tag{12}$$

The interaction between the electromagnetic fields and the surface of the nanoparticles caused by light radiation through the upper portion results in the generation of plasmons. During this interaction, carbon dioxide and water molecules are degraded. These interactions during a reaction are explained by Maxwell equations. As seen in Fig. 13a, the computed rate constant is nearly same for both simulation and experimental analysis. This demonstrates that our samples are accurately prepared and successfully synthesized without the presence of any contaminants. The findings depicted in Fig. 13b demonstrate the beneficial impact of Zn-doped WO_3 on light absorption [46]. Higher photogenerated electron/hole pairs are effectively generated owing to improved absorption, which enhances photocatalytic efficiency. The experiment yielded a similar tendency.

6 Antimicrobial Activity

To reduce the danger of contamination agar-based diffusion technique is employed [47, 48] synthesized Zn-doped WO_3 having varying antibacterial activity is evaluated against both gram-positive and gram-negative bacteria [49]. A comprehensive investigation was conducted employing a

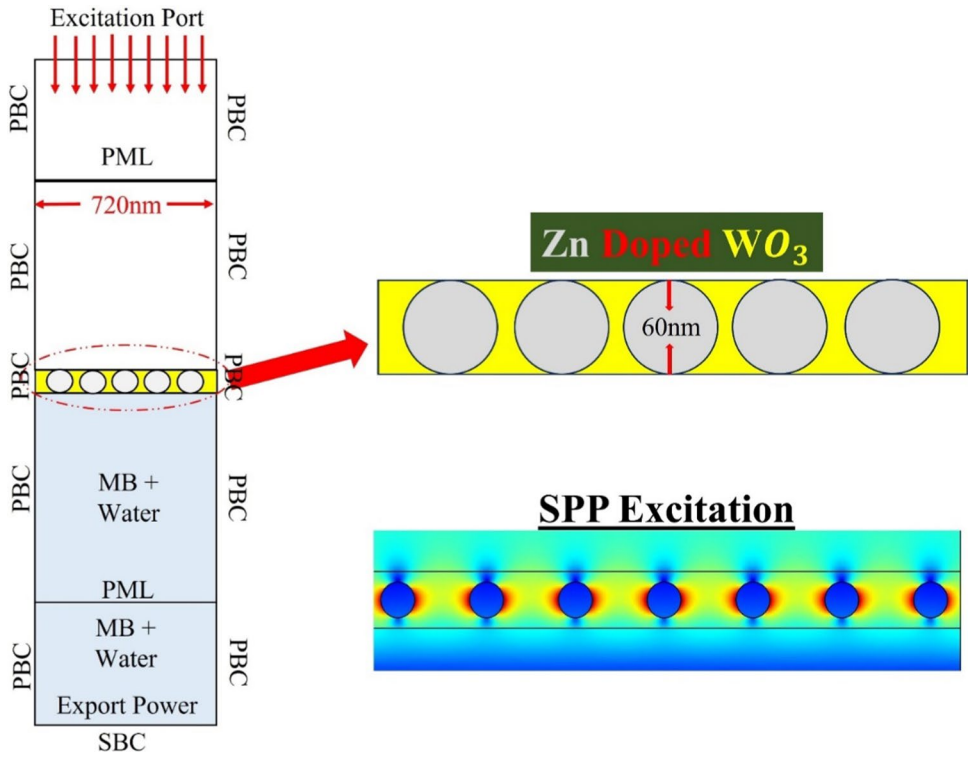

Fig. 12 2D model of Zn-doped WO_3 nanoparticles generated by the software "COMSOL," wherein the resonance frequency model illustrates the interactions between the nanoparticles and the electric field

total of 3 distinct strains of bacteria and fungi. These strains included Staphylococcus aureus (referred to as *S. aureus*), *Escherichia coli* (commonly known as *E. coli*), [50]which are both classified as Gram-negative, and *B.subtills*, classified as Gram-positive as shown in Fig. 14a. Additionally, disc diffusion was employed to assess the antifungal efficacy against 3 distinct fungal species, namely Aspergillus niger, A.glaucus, and Candida albicans as shown in Fig. 14b.

By using an array of biochemical experiments, each strain of bacteria is identified via procedure provided [51–53]. The Zn-doped WO_3,materials' antimicrobial properties against the 3 bacterial strains are examined with 2 g-negative (*S. aureus* and *E.coli*) and positive (*B.subtills*). According to

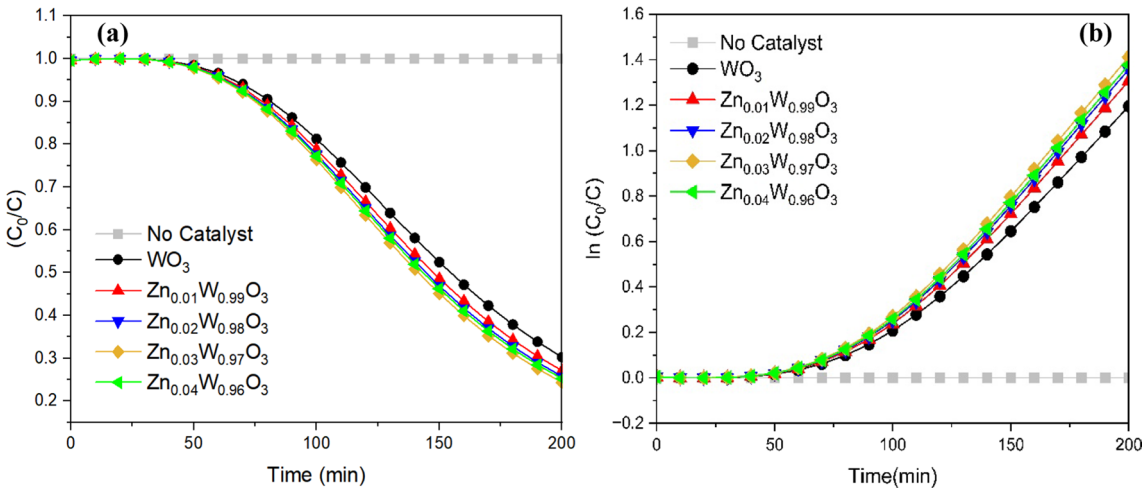

Fig. 13 **a** Simulated Zn-doped and pure WO_3 nanoparticle degradation efficiency with respect to time **b** First-order kinetics of both types of nanoparticles

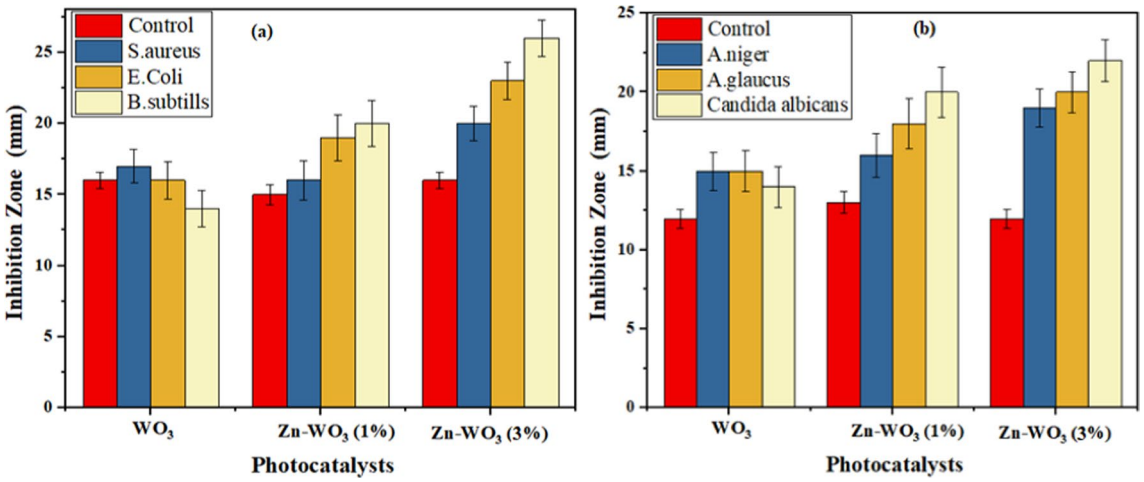

Fig. 14 Bar graph showing the diameter of the zone of inhibition (in mm) produced by **(a)**. antibacterial activity **(b)** Antifungal against Pure WO_3, 1% Zn doped WO_3 and 3% Zn dopedWO_3

the findings, in every investigated scenario, Zn-doped WO_3 NPs exhibited a greater inhibition of microbial growth and increasing the concentration of Zn gave rise to ZOI and 3% Zn doped WO_3shows the maximum zone of inhibition. Furthermore, we found that Gram-negative bacteria are more vulnerable to Zn-doped WO_3 than Gram-positive bacteria. *B.subtills* produces a ZOI of 26.5 ± 0.26 mm for Zn-doped WO_3; gram-positive bacteria, while ZOI of gram-negative bacteria, E. Coli, is 23.5 ± 0.28 mm and *S.aureus*; gram-negative shows 21 ± 0.27 mm. Similarly, 3% Zn doped WO_3shows the maximum zone of inhibition against antifungal strains such as Candida albicans shows ZOI of 22 ± 0.28 mm, A. glacucus 20.5 ± 0.26 mm and A niger shows 20 ± 0.26 mm.

The Investigations shows that Zn-doped WO_3 or powders in an aqueous solution are capable of producing multiple reactive oxygen species [15] like O_2^-, (OH), and singlet oxygen [51]. Singlet oxygen species and hydroxyl radicals are negatively charged substances that are unable to pass through cell membranes [54, 55]. Microbes are eradicated by Zn^{+2}, W^{+6}, ions that are released from Zn-doped WO_3 [56]. Significant amounts of zinc ions are known to have detrimental effects on a variety of bacterial processes, including acid tolerance, glycolysis, and transmembrane proton transfer, all of which can prolong the lag phase of the bacterium [57]. Cell death may occur if Zn ions attach to DNA molecules and break the helix shape [15]. Oxidative stress brought on by ROS can damage bacterial membranes, lipids, proteins, and DNA [58]. The production of ROS by NPS, which penetrates the microbial cell membrane, causes the ejection of cytoplasmic contents. The reactivity of nanomaterials to strains of bacteria, leading to the collapse of micropathogens, could also be mediated by the tight interaction of Zn^{+2} with negatively charged portions of the bacteria's cell membrane [59, 60].

7 Conclusion

In the current study, the environmentally friendly hydrothermal synthesis method was successfully applied to synthesize pure and Zn-doped WO_3 nanoparticles in a range of concentrations of 1 to 4% for the MB dye's photocatalytic degradation. Zn has been successfully doped as evidenced by the decreased band gap, decrease in crystallinity, and minimal shift in the XRD. Doping WO_3 with Zn^{+2} ions reduce the recombination rate of photogenerated electrons due to the similar ionic radii of Zn^{+2} and WO_3 and decreases the band gap to 2.16 eV and 1.94 eV respectively. The morphology and average size of the nanoparticles (NPs) were examined using scanning electron microscopy (SEM). The photocatalytic activity and recyclability of pure and 3% Zn-doped WO_3 for the degradation of methylene blue [27] dye under visible light irradiation were investigated. The 3% Zn-doped WO_3 catalyst exhibited the highest 85% photocatalytic activity, with complete degradation of MB achieved in 120 min. This could be attributed to the strong absorption of visible light by 3% Zn-doped WO_3. A trapping experiment using different scavengers revealed that superoxide radicals ($\bullet O_2^-$) and hydroxyl radicals (•OH) contribute significantly to the MB's degradation. The results suggest a potential interaction in the photodegradation process of 3% Zn-doped WO_3 with visible electrons and holes produced by photogenerated light. The electrons react with oxygen molecules to form $\bullet O_2^-$, while the holes react with water molecules to form •OH.

The interaction of photosensitized Zn with the catalyst WO_3 has been suggested as a potential photodegradation mechanism. Moreover, COMSOL is effectively utilized to correlate the simulation results with the experimental findings. The theoretical investigation reveals that 3% Zinc doped WO_3 absorb light more effectively than pure WO_3, revealing their increased photocatalytic activity in the breakdown of organic pollutants. The Zn-doped WO_3 exhibited notable antibacterial efficacy against *Staphylococcus aureus*, *Escherichia coli*, and *B.subtills*, additionally, antifungal activity was also examined. The observed results indicate that the Zn-doped WO_3material did not exhibit significant efficacy in inhibiting the growth of Aspergillus niger, A.glaucus, and Candida albicans. However, it is noteworthy that the Zn-doped WO_3 showed notable antimicrobial activity against bacterial strains. Zn-doped nanomaterials research has very exciting future potential for photocatalytic and antibacterial applications. Advancements and developments in this area could results in more effective, efficient and sustainable methods of medical sterilization equipment and water purification.

Acknowledgements Dr Tahir Iqbal (Principal Investigator) greatly acknowledge the financial support from Higher Education Commission (HEC), Pakistan through NRPU project no. 14755.

Author Contributions Huma Tabassum contributed about conceptualization, methodology and original/initial draft, Tahir Iqbal contributed towards conceptualization, formal analysis and Supervision, validation and review and editing. Both Authors read and approved the manuscript.

Funding "Higher Education Commission (HEC), Pakistan through NRPU project no. 14755."

Availability of Data and Materials "All data generated or analyzed during this study are included in this published article."

Declarations

Competing Interests "Yes, the project is sponsored by "Higher Education Commission (HEC), Pakistan through NRPU through project no. 14755".

Ethical Approval "Not applicable."

Consent to Participate "Not applicable."

Consent to Publish "Not applicable."

References

1. X. Xu, H. Yang, C. Li, Theoretical model and actual characteristics of air pollution affecting health cost: a review. Int. J. Environ. Res. Public Health. **19**(6), 3532 (2022)
2. P. González-Borrero et al., Optical band-gap determination of nanostructured WO3 film. Appl. Phys. Lett. (2010). https://doi.org/10.1063/1.3313945
3. H.R. Khakhal et al., Correlation of oxygen defects, oxide-ion conductivity and dielectric relaxation to electronic structure and room temperature ferromagnetic properties of Yb3+ doped CeO2 nanoparticles. Mater. Sci. Eng. B **297**, 116675 (2023)
4. S. Ibrahim et al., Adsorption of anionic dyes in aqueous solution using chemically modified barley straw. Water Sci. Technol. **62**(5), 1177–1182 (2010)
5. A. Hashem et al., Adsorbent based on agricultural wastes for heavy metal and dye removal: A review. Energy Educ. Sci. Technol **19**(69), e86 (2007)
6. K.A. Adegoke, O.S. Bello, Dye sequestration using agricultural wastes as adsorbents. Water Resour. Indus. **12**, 8–24 (2015)
7. M.C.M. Ribeiro et al., Textile wastewater reuse after additional treatment by Fenton's reagent. Environ Sci. Pollut. Res. **24**, 6165–6175 (2017)
8. P. Sarojini et al., Design of V2O5 blocks decorated with garlic peel biochar nanoparticles: a sustainable catalyst for the degradation of methyl orange and its antioxidant activity. Materials **16**(17), 5800 (2023)
9. R.D. Cortright, R. Davda, J.A.J.N. Dumesic, Hydrogen from catalytic reforming of biomass-derived hydrocarbons in liquid water. Nature **418**(6901), 964–967 (2002)
10. P. Surendran et al., Fluorescent carbon quantum dots from Ananas comosus waste peels: a promising material for NLO behaviour, antibacterial, and antioxidant activities. Inorg Chem Commun **124**, 108397 (2021)
11. K. Kannan et al., Y3+ and Sm3+ co-doped mixed metal oxide nanocomposite: Structural, electrochemical, photocatalytic, and antibacterial properties. Appl. Surf. Sci. Adv. **4**, 100085 (2021)
12. K. Kannan et al., Facile fabrication of novel ceria-based nanocomposite (CYO-CSO) via co-precipitation: Electrochemical, photocatalytic and antibacterial performances. J Mol Str **1256**, 132519 (2022)
13. M. Rezayeenik, M. Mousavi-Kamazani, S. Zinatloo-Ajabshir, CeVO4/rGO nanocomposite: facile hydrothermal synthesis, characterization, and electrochemical hydrogen storage. Appl. Phys. A **129**(1), 47 (2023)
14. X.-Q. Qiao et al., In situ synthesis of n–n Bi 2 MoO 6 & Bi 2 S 3 heterojunctions for highly efficient photocatalytic removal of Cr (vi). J Mater Chem A **6**(45), 22580–22589 (2018)
15. D. Monteiro et al., Silver colloidal nanoparticles: effect on matrix composition and structure of Candida albicans and Candida glabrata biofilms. J. Appl. Microbio **114**(4), 1175–1183 (2013)
16. H.-Y. Liu et al., Facile assembly of g-C3N4/Ag2CO3/graphene oxide with a novel dual Z-scheme system for enhanced photocatalytic pollutant degradation. Appl. Surf. Sci. **475**, 421–434 (2019)
17. K. Kannan et al., Photocatalytic, antibacterial and electrochemical properties of novel rare earth metal oxides-based nanohybrids. Mater. Sci. Energy **3**, 853–861 (2020)
18. Y. Gun et al., Joint effects of photoactive TiO2 and fluoride-doping on SnO_2 inverse opal nanoarchitecture for solar water splitting. ACS Appl. Mater. Interf. **7**(36), 20292–20303 (2015)
19. S. Liew et al., Yb-doped WO3 photocatalysts for water oxidation with visible light. Int. J. Hydrog. Energy **39**(9), 4291–4298 (2014)
20. M.B. Tahir et al., Nanostructured-based WO 3 photocatalysts: recent development, activity enhancement, perspectives and applications for wastewater treatment. Int. J. Environ. Sci. Technol. **14**, 2519–2542 (2017)
21. I. Aslam et al., The synergistic effect between WO 3 and gC 3 N 4 towards efficient visible-light-driven photocatalytic performance. New. J. Chem. **38**(11), 5462–5469 (2014)
22. C.L. Zhang, J.J. Li, S.Y. Li, Photocatalytic degradation of pefloxacin in water by modified nano-zinc oxide. Mater. Lett. **206**, 146–149 (2017)

23. L.T. Nguyen et al., Preparation, characterization and photocatalytic activity of La-doped zinc oxide nanoparticles. Materials **12**(8), 1195 (2019)
24. K. Kasinathan et al., Photodegradation of organic pollutants RhB dye using UV simulated sunlight on ceria based TiO2 nanomaterials for antibacterial applications. Sci. Rep. **6**(1), 38064 (2016)
25. M. Sasmaz, E. Obek, A. Sasmaz, The accumulation of La, Ce and Y by Lemna minor and Lemna gibba in the Keban gallery water, Elazig Turkey. Water Environ. J. **32**(1), 75–83 (2018)
26. A. Alasadi, F. Khaili, A.J.C.I. Awwad, Adsorption of Cu (II), Ni (II) and Zn (II) ions by nano kaolinite: thermodynamics and kinetics studies. Chem. Int. **5**(4), 258–26 (2019)
27. P. Shandilya et al., Properties, optimized morphologies, and advanced strategies for photocatalytic applications of WO3 based photocatalysts. J. Hazardous Mater. **428**, 128218 (2022)
28. A. Younas et al., Experimental and theoretical comparative analysis of pure WO3 and La doped WO3 for degradation of MB. Optic. Quant. Electron. **55**(13), 1172 (2023)
29. I. Maryam et al., Synthesis and characterization of ta-doped WO3 nanomaterials for their application as an efficient photocatalyst. J. Inorgan. Organomet. **33**(11), 3454–3467 (2023)
30. P. Anusha Kumari et al., Evaluation of Zn: WO3 thin films as a sensing layer for detection of NH3 gas. Micromachines **14**(4), 732 (2023)
31. J. Guo et al., Synthesis of WO 3@ Graphene composite for enhanced photocatalytic oxygen evolution from water. RSC Adv. **2**(4), 1356–1363 (2012)
32. P. Scherrer, Bestimmung der Grosse und inneren Struktur von Kolloidteilchen mittels Rontgenstrahlen. Nach Ges Wiss Gottingen **2**, 8–100 (1918)
33. E.F.A. Zeid et al., The effect of CdO content on the crystal structure, surface morphology, optical properties and photocatalytic efficiency of p-NiO/n-CdO nanocomposite. Results Phys. **12**, 562–570 (2019)
34. S.S. Wagh, C.V. Jagtap, V.S. Kadam, S.F. Shaikh, M. Ubaidullah, P. Bidhan, D.B. Salunkhe, R.S. Patil, Silver doped ZnO nanoparticles synthesized for photocatalysis application. ES Energy Environ. **17**, 94–105 (2022)
35. R.F. Wilson, Nanotechnology: the challenge of regulating known unknowns. J. Law Med. Ethics **34**(4), 704–713 (2006)
36. M. Arshad et al., Zn-doped SiO2 nanoparticles preparation and characterization under the effect of various solvents: antibacterial, antifungal and photocatlytic performance evaluation. J. Photochem. Photobio. B Biol. **185**, 176–183 (2018)
37. M. Arshad et al., Influence of different solvents on portrayal and photocatalytic activity of tin-doped zinc oxide nanoparticles. J. Mol. Liquids **260**, 272–278 (2018)
38. X. Xu et al., Sol–gel synthesis and enhanced photocatalytic activity of doped bismuth tungsten oxide composite. Mater. Res. Bull. **73**, 385–393 (2016)
39. I. Bibi et al., Green and eco-friendly synthesis of cobalt-oxide nanoparticle: Characterization and photo-catalytic activity. Adv. Powder Technol. **28**(9), 2035–2043 (2017)
40. X. Cheng et al., Enhanced photoelectrocatalytic performance of Zn-doped WO3 photocatalysts for nitrite ions degradation under visible light. Chemosphere **68**(10), 1976–1984 (2007)
41. T.T. Nguyen et al., Tungsten trioxide (WO3)-assisted photocatalytic degradation of amoxicillin by simulated solar irradiation. Sci. Rep. **9**(1), 9349 (2019)
42. M.A.M. Khan, et al., Hydrothermally produced Mo-doped WO3 nanoparticles and their enhanced photocatalytic and electrochemical properties (2023)
43. M.H. Sayed Abhudhahir, J. Kandasamy, Photocatalytic effect of manganese doped WO3 and the effect of dopants on degradation of methylene blue. J. Mater. Sci. Mater. Electron. **26**(11), 8307–8314 (2015)
44. L. Lovisa et al., Synthesis of Pr 3+-doped WO 3 particles: correlation between photoluminescent and photocatalytic properties. RSC Adv. **13**(37), 25738–25751 (2023)
45. H. N. Köysüren, Ö. Köysüren, Improving UV light photocatalytic activity of WO3 by doping with boron and compounding with polypyrrole. (2022)
46. R. Ebrahimi et al., Photocatalytic degradation of organic dyes using WO3-doped ZnO nanoparticles fixed on a glass surface in aqueous solution. J. Indust. Eng. Chem. **73**, 297–305 (2019)
47. C. Valgas et al., Screening methods to determine antibacterial activity of natural products. Brazil. J. Microbiol. **38**, 369–380 (2007)
48. K. Chinnaiah et al., Exploring the potential of Withania somnifera-mediated Ag/Mn3O4 nanocomposites as electrode material for high-performance supercapattery device. J. Taiwan Instit. Chem. Eng. **157**, 105441 (2024)
49. K. Chinnaiah et al., Ag nanoparticles synthesized by Datura metel L. Leaf extract and their charge density distribution, electrochemical and biological performance. Chem. Phys. Lett. **807**, 140083 (2022)
50. P. Sasikumar et al., Evaluating the antimicrobial and electrochemical performance of phenytoin nanoparticles from Catharanthus roseus plant. Chem. Phys. Lett. **839**, 141111 (2024)
51. A. Lipovsky et al., EPR study of visible light-induced ROS generation by nanoparticles of ZnO. J. Phys. Chem. C. **113**(36), 15997–16001 (2009)
52. V. Revathi, K.J.C.D.C. Karthik, Physico-chemical properties and antibacterial activity of Hexakis (Thiocarbamide) Nickel (II) nitrate single crystal. Chem. Data Collect. **21**, 100229 (2019)
53. S. T. Cowan, Cowan and Steel's manual for the identification of medical bacteria. Cambridge University Press. (1993)
54. K. Chinnaiah et al., Nanostructured Ag/NiO composites for supercapacitor and antibacterial applications, and in-silico theoretical investigation. J. Phys. Chem. Solids **184**, 111730 (2024)
55. N. Padmavathy, R.J.S. Vijayaraghavan, Enhanced bioactivity of ZnO nanoparticles—an antimicrobial study. Sci. Technol. Adv. Mater. (2008). https://doi.org/10.1088/1468-6996/9/3/035004
56. I.A. Hassan et al., Antimicrobial properties of copper-doped ZnO coatings under darkness and white light illumination. ACS Omega **2**(8), 4556–4562 (2017)
57. G. Applerot et al., Coating of glass with ZnO via ultrasonic irradiation and a study of its antibacterial properties. Appl. Surf. Sci. **256**(3), S3–S8 (2009)
58. K. Chinnaiah et al., Datura metel L. leaf extract mediated sodium alginate polymer membrane for supercapacitor and food packaging applications. Int. J. Biol. Macromol. **242**, 125112 (2023)
59. M. Gohulkumar et al., Enhanced cytotoxicity and apoptosis-induced anticancer effect of silibinin-loaded nanoparticles in oral carcinoma (KB) cells. Mater. Sci. Eng. C. **41**, 274–282 (2014)
60. K. Gurushankar et al., Synthesis, characterization and in vitro anti-cancer evaluation of hesperetin-loaded nanoparticles in human oral carcinoma (KB) cells. Adv. Nat. Sci. Nanosci. Nanotechnol. **5**(1), 015006 (2013)